HHS Public Access

Author manuscript

Exp Eye Res. Author manuscript; available in PMC 2017 December 01.

Published in final edited form as:

Exp Eye Res. 2016 December ; 153: 65–78. doi:10.1016/j.exer.2016.10.001.

The Adult Zebrafish Retina: *In Vivo* Optical Sectioning with Confocal Scanning Laser Ophthalmoscopy and Spectral-Domain Optical Coherence Tomography

Brent A. Bell[1], **Alex Yuan**[1,2], **Rose M. Dicicco**[1], **Joseph Fogerty**[1], **Emma M. Lessieur**[1,3], and **Brian D. Perkins**[1,2]

[1]Ophthalmic Research, Cole Eye Institute, Cleveland Clinic, Cleveland, OH

[2]Department of Ophthalmology, Cleveland Clinic Lerner College of Medicine of Case Western Reserve University, Cleveland, OH

[3]Molecular Medicine PhD Program Cleveland Clinic Lerner College of Medicine of Case Western Reserve University, Cleveland, OH

Abstract

Non-invasive imaging is an invaluable diagnostic tool in ophthalmology. Two imaging devices, the scanning laser ophthalmoscope (SLO) and spectral domain optical coherence tomography (SDOCT), emerged from the clinical realm to provide research scientists with a real-time view of ocular morphology in living animals. We utilized these two independent imaging modalities in a complementary manner to perform *in vivo* optical sectioning of the adult zebrafish retina. Due to the very high optical power of the zebrafish lens, the confocal depth of field is narrow, allowing for detailed *en face* views of specific retinal layers, including the cone mosaic. Moreover, we demonstrate that both native reflectance, as well as fluorescent features observed by SLO, can be combined with axial in-depth information obtained by SDOCT. These imaging approaches can be used to screen for ocular phenotypes and monitor retinal pathology in a non-invasive manner.

Introduction

Confocal Scanning Laser Ophthalmoscopy (SLO) and Spectral Domain Optical Coherence Tomography (SDOCT) have now become widespread tools for basic vision research. Both instruments enable non-invasive, *in vivo* assessment of ocular tissues from a multitude of animal species. *In vivo* assessments have previously demonstrated that abnormal phenotypes may arise in both mammals and zebrafish that are present prior to the initiation of experimental studies (Bell et al., 2015; Bell et al., 2012; Joshi et al., 2016; Mattapallil et al., 2012; Tschopp et al., 2010). Using these instruments to screen for baseline abnormalities will avoid the potential for unexpected, confusing and confounding experimental results.

Corresponding Author: Brent A. Bell, Cole Eye Institute, 9500 Euclid Ave. /i31, Cleveland, Ohio 44195; Phone: (216) 445-5832; bellb3@ccf.org.

SLO, introduced for patient use in the early ‘90s, has become an important diagnostic imaging tool for ophthalmologists (Hassenstein and Meyer, 2009). Over the past decade this instrument has found widespread use in non-clinical research for imaging numerous animal models such as non-human primates (Rosolen et al., 2001), canines (Rosolen et al., 2001), swine (Rosolen et al., 2001), rodents (Hossain et al., 1998; Seeliger et al., 2005), and fish (DiCicco et al., 2014; Hossain et al., 1998; Rosolen et al., 2001; Seeliger et al., 2005). SLO has several operating modes and wavelength combinations that provide some advantages over broadband visible light fundus imaging (Bell et al., 2014), including the ability to trace fluorescent tagged cells or proteins *in vivo*. Many groups have demonstrated the ability to visualize a wide array of unique pathology and/or anatomical features using SLO. Such features include abnormal ocular phenotypes (Chauhan et al., 2012; Samuels et al., 2013), age-related or light induced changes (Bell et al., 2015; Sparrow et al., 2013), vascular angiography (Paques et al., 2006; Seeliger et al., 2005), labeled proteins (Beck et al., 2010; Seeliger et al., 2005), inflammatory cells (Paques et al., 2006), and apoptotic cells (Maass et al., 2007).

Imaging data obtained via SLO is primarily a two-dimensional (x-y), *en face* view of the posterior globe. Image acquisition refresh rates are fast enough to permit rapid screening to search quickly for abnormalities. A z-axis focus adjustment is available to accommodate varying axial lengths in human eyes. In small animals, this feature can be exploited to obtain three-dimensional information from the retina by imaging multiple planes along the z-axis in a manual, non-automated manner.

Three-dimensional information from the retina is more easily and readily collected using Spectral Domain Optical Coherence Tomography (SDOCT). SDOCT provides cross-sectional morphological information similar to that obtained by histology. Similar to SLO, SDOCT has also been widely applied to basic research in a vast array of animals including non-human primates (McLellan and Rasmussen, 2012; Toth et al., 1997), swine (Gloesmann et al., 2003), rodents (Boudard et al., 2010; Jiao et al., 2007), birds (Rauscher et al., 2013), fish (Rao et al., 2006) and amphibians (Zhang et al., 2013). However, SDOCT is limited in its utility as a research tool because it cannot detect and/or display fluorescent-tagged cells. In its current state, SDOCT relies solely on native tissue reflectance properties, originating from differences in refractive index, to provide signal contrast.

Combining the information obtained via SLO and SDOCT has tremendous advantages over using these instruments in a stand-alone manner. Capitalizing on the potential of an integrated device, manufacturers have launched combined modality systems into the clinical marketplace. Although these devices have proven useful in humans, and to some extent in small mammals, no one has demonstrated applicability of these combined modality devices in the fish eye.

We have previously demonstrated that *in vivo* transpupillary imaging of the adult zebrafish retina (*Danio rerio*) is feasible using commercially available, standalone SLO and SDOCT imaging systems (Bell et al., 2014; DiCicco et al., 2014). More specifically, this work focused on quantifying vascular leakage and laser-induced thermal injury. In this

manuscript, we describe methods to use SLO and SDOCT in a synergistic manner to perform *in vivo* optical sectioning of the retina, including detection of targeted cells.

Zebrafish have long been a favored genetic model for developmental biologists, but the increasing popularity of TALENS and CRISPR/Cas9 technologies now permits the development of adult zebrafish models of human eye diseases (Bilotta and Saszik, 2001; Chhetri et al., 2014; Hughes, 2013; Hwang et al., 2013). These models will require advanced tools and techniques for *in vivo* assessment of ocular tissues. SLO and SDOCT are valuable tools in other animal models and this work suggests this trend may continue as we further expand the role of these two imaging modalities in zebrafish vision research.

Materials and Methods

Experiments conformed to the ARVO Statement for Care and Use of Animals in Ophthalmology and Visual research. The Cleveland Clinic Lerner College of Medicine Institutional Animal Care and Use Committee approved all experimental procedures. Adult zebrafish (≥3 months) were employed for all imaging experiments. The various zebrafish lines investigated are shown in Table 1. Animals were maintained at 28.5°C on a 14-hour light/10-hour dark cycle according to standard procedures (Westerfield, 2007). Zebrafish imaging methods and animal preparatory procedures have been previously reported in detail (Bell et al., 2014; DiCicco et al., 2014). All experiments utilized light-adapted animals.

SLO & OCT Imaging Instruments

The details of the HRA2 SLO system (Heidelberg Engineering USA, Inc.) modified and applied to zebrafish imaging have been previously published (Bell et al., 2014; DiCicco et al., 2014). When using the HRA2 with the 55° wide field lens, the z-module setting can be adjusted to provide a focus range more suitable for imaging zebrafish (Suppl. Fig. 1).

Briefly, SLO images were obtained using Reflectance (“R”) and Angiography (“A”) Operating Modes. Within each mode are individual sub-modes including Infrared (IR), Infrared Dark Field (IRDF), Red Free Dark Field (RFDF), Fluorescein Angiography (FA) and Indocyanine Green Angiography (ICGA). In the absence of injected contrast agents (e.g. Sodium Fluorescein and Indocyanine Green), FA and ICGA sub-modes are often referred to as Autofluorescence (AF) and Infrared Autofluorescence (IRAF). The FA channel is sensitive enough to collect green fluorescent protein (GFP) information from the zebrafish retina.

Two SDOCT instruments were used to obtain images of the retina. The first system (SDOIS, Bioptigen, Inc. Morrisville, NC) has a center operating wavelength of ~840nm, spectral bandwidth of 65nm, and a theoretical, axial resolution of ~3.5/4.8 μm (tissue/air). With this system, imaging data was collected at a 20 kHz line rate using InVivoVue Clinic Software v1.3. The second SDOCT system was a faster (75 kHz line rate), custom-built instrument operating under InVivoVue Clinic Software v2.2.22 with a center wavelength of ~820 nm, spectral bandwidth of 150 nm and theoretical, in-depth resolution of ~1.5/2 μm (tissue/air).

Images were collected with the 50° field of view (FOV) mouse bore objective which offers a reported lateral resolution of ~2.5μm (Bioptigen, Inc.). General imaging of the retina was performed using the 3.5 μm SDOCT system and included the following scan parameters: (1) Central View - Radial Scan @ 0 & 90°, 1000 A-scans/B-scan × 10 Frames and Volume Scan @ 300 B-Scans/Volume × 100 A-scans/B-scan, (2) Peripheral Temporal and Nasal Views - Linear Scan @ 90°, 1000 A-scans/B-scan and Volume Scan @ 300 B-Scans/Volume × 300 A-scans/B-scan. With the 1.5 μm SDOCT system, higher density scans (3000 A-scan/B-scan) were employed to better reveal morphological detail within the outer retina.

Post-image Acquisition Processing

SLO images were exported as TIFF files. ImageJ (v1.47b) image processing software was used to remove the scale bars displayed in the HRA2 images because they are not calibrated for zebrafish. ImageJ was used to enhance brightness and/or contrast of some images post collection to accentuate structural detail. SDOCT images showing outer retina morphology were unaveraged and exported as bitmaps (Fig. 2, 3, 5, & 6). SDOCT images collected with the 3.5 μm system (Fig. 1 & Suppl. Fig. 3) were exported as AVI files (640 × 480 pixels by 30 B-scan frames) and opened in ImageJ. The 10 best B-scans (i.e. void of motion artifact) were selected and co-registered using the StackReg Plugin Algorithm with Rigid Body Transformation (P. Thévenaz, 1998). Finally, the average intensity from the co-registered stack was obtained (*Image>Stacks>Z project…*).

SLO Focus Span and Focus Translation Rate

Infrared SLO and SDOCT images of the dorsal retina were acquired from wild type zebrafish (n=3), BALB/cJ mice (n=13) and Long-Evans rats (n=4) to compare and contrast focus span and focus translation rate among the three different species. SLO focal position is displayed in units of refractive power (i.e. diopters). IR-SLO images were acquired from two primary reference locations (i.e. L1 & L2) within the retina. In rodents, the locations included the vitreoretinal (L1) and RPE-choroid (L2) interfaces, both regions of high signal contrast that can be easily and reliably identified. Reference locations for zebrafish also included the vitreoretinal interface (L1) but instead utilized the vitreal aspect of the cone mosaic for L2 rather than the RPE-choroid interface due to the difficulty in imaging this structure in pigmented animals. The focus span was calculated by taking the absolute difference between these two reference locations as shown in the following equation:

$$|\mathrm{SLO}\ \ \mathrm{Focus}\ \ \mathrm{Span}(D)| = L2^{\mathrm{SLO}} - L1^{\mathrm{SLO}}$$

Focus translation rate, which is the distance over which the SLO focus moves per unit diopter, was determined by incorporating axial measurements acquired by SDOCT volume scans. Depth measurements were taken by SDOCT from the same respective reference locations used to determine the focus span. The SLO focus translation rate was calculated based on the following equation for the three different species:

$$\text{SLO Focus Translation Rate}(\mu m/D) = \frac{(L2^{\text{SDOCT}} - L1^{\text{SDOCT}})}{|\text{SLO Focus Span}|}$$

Estimated SLO Image Lateral Resolution

Lateral image resolution was measured from four different lenses with increasing refractive power using a 1951 USAF High-resolution target (Edmund Optics, Barrington NJ) mounted to a XYZ translation stage (Thorlabs, Newton NJ). Three lenses were plano-convex with the following characteristics 167 D (3 mm ø × 6 mm FL), 333 D (3 mm ø × 3 mm FL), and 667 D (2 mm ø × 1.5 mm FL). One lens with the highest refractive power (1363 D) was made to mimic the cornea and lens of the zebrafish eye. This lens was spherical (1 mm ø × 0.734 mm FL) and was cemented directly to a 0.9 mm (ø) precision pinhole (Edmund Optics, Barrington NJ). Averaged (25 frames) IR images of the resolution target were exported to ImageJ where longitudinal profiles were obtained of the calibrated rulings. Modulation Transfer Function (MTF) was calculated using the following equation:

$$\text{MTF}\left(\frac{\text{lines}}{\text{mm}}\right) = (I^{\max} - I^{\min})/(I^{\max} + I^{\min})$$

Estimated SLO Confocal Depth of Field

Confocal depth of Field (DOF) was measured using the same experimental set up employed to obtain lateral resolution except the high resolution target was substituted with a 1mm thick microscope slide and 0.1 mm cover slip with a 30 µl drop of 0.0003% Sodium Fluorescein sandwiched between the slide and cover slip. DOF was measured by mounting the slide sandwich to the XYZ translation stage and advancing it through the SLO image plane using a precision micrometer. Images were collected at a 25° FOV using AF-SLO with a fixed signal gain set to 70 and without automatic image intensity normalization. Imaging data obtained in triplicate were exported to ImageJ where each image panel was measured for average intensity. Data obtained from triplicate measures of each lens were averaged and inserted into Graphpad Prism (Graphpad Software, La Jolla, CA) where a cubic spline curve was generated. The cubic spline data were normalized to display the data as signal amplitude versus depth of field for the four glass lenses of increasing refractive power.

Data Processing and Statistics

GraphPad Prism 6 was used for graphical display and statistical analysis of data. P-values of 0.05 or less was considered significant. Chromatic aberration data was analyzed using a paired one-tailed t-test or repeated measures one-way ANOVA corrected with a Tukey's multiple comparisons test.

Results

SLO & SDOCT Imaging of the Zebrafish Retina

Representative SLO and SDOCT images from wild-type and albino zebrafish are shown in Fig. 1. By using IR- and IRDF-SLO, two specific imaging planes containing discernible features are observed within the inner and outer retinal regions. In the inner retina, the vitreoretinal interface (VRI) could be best visualized by IR-SLO (Figs. 1A, D). At this location, vasculature and nerve fiber bundles were observed emerging from the optic disk and extending peripherally. For the outer retina, a speckled pattern, suspected to be photoreceptors or RPE, could be identified using both IR (not shown) and IRDF-SLO (Figs. 1B, E). IRDF mode, which is absent of objective lens reflection artifact, was much better at revealing this particular feature. Finding this outer retinal plane was more difficult in albino animals (Fig. 1E). In pigmented animals, no additional morphological detail could be resolved beyond this speckled zone. In albino animals, however, additional detail could be visualized beyond this location, although these structures could not be positively identified (i.e. as RPE, choroid, photoreceptor rods, etc.).

The speckled pattern in the outer retina is likely photoreceptors and pigmentation from the underlying RPE. In this plane, a hyper-reflective oblong ring circumscribing the optic disk (Fig. 1B and 1G, hashed white line) corresponds to the larval remnant of photoreceptors (Allison et al., 2010; Duval et al., 2013). The long axis was always oriented in the dorsal-ventral direction (Fig. 1B, G). Using IRDF-SLO, the cone photoreceptor mosaic was most easily visualized outside this ring as rows that extend linearly outward from the optic nerve (Fig. 1G – see peripheral images from dorsal, nasal, ventral and caudal regions). Intercalated photoreceptors (Fig. 1G-ROI_{out}; white dotted lines) can be observed inserted between existing photoreceptor rows (Fig. 1G-ROI_{out}; black dotted lines). Within the larval remnant, however, photoreceptors were seen as dark circular patches distributed within the image frame and lacking an organized pattern (Fig. 1G-ROI_{IN}).

At either one of the inner and outer retina image planes, AF- (Figs. 1C & 1F) or IRAF-SLO (not shown) can be performed to obtain autofluorescence information from the same plane as those collected for IR- and IRDF-SLO. AF-SLO signal from native, endogenous fluorophores within the zebrafish retina was extremely weak and required maximized signal gain settings (107; range 35-107) and frame co-registration and averaging (ART~25) to acquire information. AF images from albino and pigmented animals were similar (Figs. 1C, 1F) and resemble those previously shown in mice (Charbel Issa et al., 2013; Sparrow et al., 2013). In contrast, signal from GFP and EGFP positive expressing targets are more robust (Suppl Fig. 2). Animals expressing GFP required gain settings somewhat similar to those that are unlabeled with GFP (95-100 vs. 107). Strains expressing EGFP required less than half the gain than those with GFP (40-50 vs. 95-100).

A major limitation observed using both IRDF- and AF-SLO was the inability to delineate morphological detail from within the cone mosaic. We were unable to distinguish between rods, cones, and different types of cones. Nevertheless, distinguishable features were often observable within the retina from different zebrafish lines that would yield some useful information on GFP expression and structural morphology (Suppl. Fig. 2).

An example of the utility of combining this information with SDOCT is demonstrated in Supplemental Figure 3A-J. Even with the aforementioned limitations in resolving power, native abnormalities could be distinguished between abnormal (Suppl. Fig. 3F-J) vs. normal (Suppl. Fig. 3A-E) *Tg(-3.2gnat2:EGFP)* animals. This particular transgenic strain was observed to have abnormalities, the majority bilateral, about 30% of the time whereas other strains ranged from 2 to ~15% (Suppl. Fig. 3K).

SDOCT B-scans through the optic nerve show similarities and differences between the retinal morphology of pigmented wild type and albino zebrafish (Figs. 1H, I). Hashed black horizontal lines indicate the approximate location where the IR-SLO images (Figs. 1A, C) were obtained from the VRI in the inner retina. Hashed-dot-dot black horizontal lines indicate the approximate location where IRDF-SLO images (Figs. 1B, E) were acquired from the outer retina. B-scans obtained from albino animals (Fig. 1I) were similar to pigmented animals (Fig. 1H) with exception to the distal aspect of the outer retina. As previously demonstrated by Bailey et al. (Bailey et al., 2012)., additional bands (Figs. 1H, I-white double brackets) can be observed in the outer retina beyond the bright reflective band in the albino (Fig. 1I) vs. pigmented (Fig. 1H) animals. This feature is better accentuated using a longitudinal reflectance profile (LRP). In the LRP, two smaller but distinct peaks (arrow) can be seen in albinos but not in pigmented animals. These peaks are believed to represent rod outer segments (ROS) and the retinal pigment epithelium (RPE) (Bailey et al. 2012).

Bailey et al previously correlated SDOCT in-depth reflectance architecture to histology from radial sections and indicated the locations of the ganglion cell layer (GCL), inner nuclear layer (INL) within the inner retina and the outer nuclear layer (ONL) and photoreceptor outer segments (OS) in the outer retina (Bailey et al., 2012). Unlike humans, the zebrafish outer retina consists of multiple types of photoreceptors arranged in a tiered, crystalline-like manner (Branchek and Bremiller, 1984; Raymond et al., 1995; Robinson et al., 1993). To accurately correlate outer retinal anatomy with SDOCT in-depth reflectance, we imaged several *Tg(-3.2gnat2:EGFP)* animals using two different imaging systems. It has been shown theoretically in humans that proximal photoreceptor outer segments (1st surface near the IS/OS junction), and distal/apical tips (a.k.a. cone outer segment tips; “COST”) are the source of bright reflective SDOCT signal in the photoreceptor layer (Jonnal et al., 2010; Pallikaris et al., 2003; Zhang et al., 2006). After viewing SDOCT *en face* and B-scan images of the zebrafish retina, we hypothesized that transitions between photoreceptor inner/outer segments are responsible for the multiple reflectance bands seen in zebrafish. A series of imaging experiments was performed using two independent SDOCT systems to test this hypothesis (Fig. 2).

SDOCT at 3.5 μm resolution shows the outer retina as a region of alternating signal of bright and dark bands (Fig. 2A). Bright, punctate, and asymmetrically elongated foci were observed within this region. Magnification of the outer retina and an LRP reveals foci aligned in multiple, horizontally oriented axes (Figs. 2B-C; dotted lines aligned to image margins). The upper-most line observed in Fig. 2B appears to be the external limiting membrane (ELM) since it is juxtaposed to the dark band denoting the ONL. Displacement of the ELM is observed in the far right half of the image (Fig. 2B, Δz), which can likely be

attributed to motion artifact (i.e. operculum movement). White arrowheads indicate reflections from the IS/OS interface (e.g. proximal aspect) and apical tip (e.g. distal aspect) of a cone photoreceptor outer segment (OS), respectively. The axial depth, shown relative to the external limiting membrane for reference, indicates that the distance between the two reflections is ~10 μm. The axial distance occupied by cone photoreceptors (Figs. 2A-B: yellow bar) and rod outer segments (Fig. 2A; maroon bar) was ~40 and 25 μm in length, respectively (Fig. 2A-B), which agrees with previously published measurements obtained from semi-thin histological sections (Branchek and Bremiller, 1984). Light and dark adaptation influences RPE melanosome location and movement between basal and apical locations depending on light condition (Hodel et al., 2006). In this light-adapted animal, the melanin pigment band (MPB) was observed to be ~ 35 μm in length (Fig. 2A-B, black bar).

We used volume intensity projections (VIP) from the various laminar regions within the outer retina to show how the *en face* appearance changes relative to B-scan image depth (Figs. 2D-H). Numerous reflections (white foci) were observed in the VIP *en face* view. As the projection window advanced in the direction of the sclera, the VIP view changed from discrete, punctate short single cones (Fig. 2E) to the long single cones and double cones (Fig. 2F). Additional background signal was observed encompassing the short single cones (Fig. 2F), which reduced visualization and image contrast. The additional background observed originates from the proximal aspect of the long single cones; however, these reflections are weaker and less discernible than those from the proximal and distal aspects of short single cones. The morphology transitioned from the apical tips of the long single cones to the inner segment/outer segment transition of the double cones. In addition, melanosomes within apical RPE microvilli are extended and encompass double cones in light-adapted animals. Melanosomes contribute to an increase in background signal in the VIP and elevates the LRP signal amplitude at a depth of ~25 μm relative to the ELM (Figs. 2B-C). The brightest reflectance band was observed in the region containing the double cone outer segments along with RPE microvilli/melanosome apical extensions. The lack of melanin in albino animals appeared to increase optical penetration depth and permitted visualization of features beyond the MPB (i.e. Rod OS, RPE & choroid) in Fig 1I. Albino animals still exhibited a prominent, hyper-reflective MPB that suggests this band does not exclusively originate from melanin granules. In light of this observation it seems possible that this particular band originates from melanosomes, still present within the RPE apical extensions but unable to produce, and thus devoid of dark melanin pigment.

To more thoroughly investigate and confirm the findings we observed using the 3.5 μm axial resolution system, we performed additional imaging sessions on *Tg(-3.2gnat2:EGFP)* zebrafish using the custom built system operating with improved acquisition speed and axial resolution (Figs. 2I-J). To better convey cone and rod architecture, scale representations of short single cones (magenta), long single cones (blue), double cones (red/green) and rods (maroon) have been overlaid in the appropriate locations within the diagram of the outer retina (Fig. 2I).

In Fig. 2J, a threshold has been applied to the B-scan (Fig. 2I) to better accentuate cone proximal and distal reflections present throughout the cone mosaic. The colored arrows (down arrow: proposed IS-OS interface or proximal aspect; up arrow: proposed apical tips or

distal aspect) shown in Fig. 2J correspond to the location of the photoreceptor (SSC, LSC, and DC) representations shown in Fig. 2I. A normalized LRP of the native SDOCT image (Fig. 2I) is displayed in Fig. 2K with dotted lines used to indicate the ELM and cone basal and apical reflections. A “to scale” color diagram of photoreceptor architecture, adopted from Branchek and Bremiller, was overlaid on the LRP graph to compare outer retina reflectance architecture obtained by SDOCT with the previously reported model (Branchek and Bremiller, 1984). From this comparison, it can be seen that the morphological information obtained *in vivo* by SDOCT is in good agreement with the Brancheck and Bremiller model. The 1.5 μm system, with ~50% improved resolution and faster acquisition speed, was better equipped to resolve and delineate reflections that exist between the proximal and distal aspects of the different cone photoreceptor types. Furthermore, as shown, these observations were verified using two independent SDOCT imaging systems in more than one animal.

Calibration of SLO Axial Focus by Correlating Anatomical Reference Locations between SLO and SDOCT

SLO axial focus adjustment is displayed in units of Diopter (D). Specific anatomical sites within an animal, whether it is a mammal or fish, can be used to calibrate the instrument focus position (Bell et al., 2015). The VRI and the proximal cone mosaic, areas of significant native contrast within the retina, can be used to establish calibration endpoints. However, an important requirement to accomplish this is to have in hand complementary SDOCT information to compute a correction/scaling factor for the SLO.

In our previous work we realized, but did not report, an approximate SLO scaling for zebrafish (~1μm/Diopter) (Bell et al., 2014). To revise and obtain a more accurate estimate of this correction factor, new experiments were conducted in three *Tg(-3.2gnat2:EGFP)* animals. Figs. 3A-B show the appearance of the VRI and photoreceptors visible in the outer retina by IR-SLO, respectively. Directly below in Figs. 3C-D are SDOCT VIPs of the same anatomical features observed by IR-SLO. The VIP regions are shown bound by green lines in the in-depth B-scans (Figs. 3E-F). A longitudinal ROI, and its accompanying LRP from one animal, are displayed in Figs. 3G-H, respectively. Fig. 3H shows the SLO focus positions (mean ± stdev) for the VRI (17.3±13.2 D) and cone mosaic (-116±14.7 D) from three *Tg(-3.2gnat2:EGFP)* animals. On average, this represents an absolute SLO focus position difference of 133.3 D (Δy) between the VRI and cone mosaic reference locations. SDOCT B-scans from identical reference locations revealed a mean axial length of 115.6±5.1μm (Δx). This information was used to obtain the slope (Δy/Δx), which was -1.153 and provided a scaling/correction factor (1/slope) for the SLO axial focus position relative to Diopter reading (1 D = 0.867 μm).

The Influence of Chromatic Aberration on SLO Focus Position

Once the SLO axial focus adjustment was calibrated, pseudo-tomography could be performed by simple, manual adjustment of the SLO focus knob. In-depth sectioning could be used to capture both native reflectance and autofluorescent information from within the retina. However, before this technique could be fully deployed, additional obstacles were observed that would prevent correlation of SLO and SDOCT data. Substantial chromatic

aberration was observed between SLO channels operating at short (488 nm) vs. long (795 & 820 nm) excitation/illumination wavelengths. Fig. 4 shows the results from an experiment devised to determine the approximate amount of chromatic aberration that exists in inner and outer retina. This issue had the potential to introduce error when attempting to overlay SLO and SDOCT information.

To determine the amount of chromatic aberration, two particular zebrafish lines, *Tg(apoeb:lynEGFP)* and *Tg(-3.2gnat2:EGFP)* were selected because they have anatomical features at the two most recognizable reference points (i.e. VRI and photoreceptors) in the retina. As demonstrated in Fig. 3, the VRI and cone mosaic are very recognizable points that could be visualized both by IR- and AF-SLO imaging modes and used for calibration of SLO axial focus depth. In Figs. 4A-B, features of the VRI, primarily retinal vessels and the nerve fiber layer, can be observed by both IR- and AF-SLO in *Tg(apoeb:lynEGFP)* animals, respectively. As shown in Fig. 4C, the SLO focus positions required to visualize IR reflective features are significantly different than those observed by GFP fluorescence. The excitation lasers used for the IR modes (795 and 820nm) are similar to the one used for SDOCT (840nm). The image obtained from SLO is due to reflectance of the IR light, similar to the VIP images obtained by SDOCT. In AF mode, the SLO excitation laser (488nm) causes fluorescence of GFP signal, which is expressed in Müller glia in *Tg(apoeb:lynEGFP)* animals. At the VRI, the Müller glia fill in the gaps between the ganglion cell axons running parallel to the retinal surface. The reflectance from the NFL seen in Fig. 4A allows for visualization of the parallel fibers, whereas the fluorescence from the Müller glia in Fig. 4B surrounds the NFL. Fig. 4C shows chromatic aberration between the two operating modes which is ~36 Diopters, or ~30 μm (36 D × 0.86 μm /D =31 μm). Aberration comparisons were not obtained for IRDF- or IRAF-SLO because these modes showed no, appreciable native reflective/autofluorescence contrast at the VRI reference point.

We repeated this exercise using *Tg(-3.2gnat2:EGFP)* animals to establish whether the aberration observed at the VRI remained consistent for the outer retina. In this experiment we measured the SLO focus positions of the cone mosaic using IR- (Fig. 4D), IRDF- (Fig. 4E), and AF-SLO (Fig. 4F) imaging modes. The results of this experiment are shown in Fig. 4G and first, reveal that no significant aberration is experienced between the two infrared (IR vs. IRDF) SLO operating modes. This is not surprising considering that these two IR wavelengths are separated by only 25 nm (i.e. 795 vs. 820 nm). Secondly, as previously demonstrated in Fig. 4C, this experiment again revealed that the focus position required to view similar retinal features (e.g. in this case the photoreceptor mosaic) is significantly different for IR- vs. AF-SLO imaging modes. The aberration observed between the two IR modes and AF-SLO was ~25-28 D, which equates to a focusing displacement distance of ~20-25 μm. Thus, between the two reference points, ~ 30 to 25 μm of chromatic aberration exists at the VRI and cone mosaic locations, respectively. We anticipate that the difference (30 μm vs. 25 μm) in aberration observed between these two locations (VRI vs. cone mosaic) can be attributed to the fact that the GFP^+ short single cone nuclei, located several microns (~5 μm) proximal to the basal IS-OS interface which is the site of IR- & IRDF-SLO signal contrast, induces a slight vitreal shift in the focus position measurement obtained in *Tg(-3.2gnat2:EGFP)* vs. *Tg(apoeb:lynEGFP)* animals.

In vivo Optical Sectioning and Integration of Multimodal Imaging Information

In vivo optical sectioning was performed to characterize two zebrafish strains *Tg(apoeb:lynEGFP)* and *Tg(mpeg1:EGFP)*. *Tg(apoeb:lynEGFP)* has been previously shown to express EGFP in microglia of zebrafish brain (Peri and Nusslein-Volhard, 2008). However, we found GFP expression in the retina to be restricted to Müller glia as reported in *Tg*(*gfap:EGFP*) (Alvarez et al., 2007). Expression of GFP from *Tg(mpeg1:EGFP)* animals was found in retinal microglia.

Retinal Müller glia traverse almost the entire length of the retina from the VRI to the external limiting membrane. Thus, imaging Müller glia provides a good opportunity to optically section through the different retinal layers using SLO. Fig. 5 shows representative SLO and SDOCT images from various retinal lamina of *Tg(apoeb:lynEGFP)* zebrafish where specific morphological information could be observed. An initial pass through the retina with an SLO FOV of 55°, originating at the VRI and advancing to the photoreceptor layer, revealed 5 distinct locations (Figs. $5A_0$-$4F_0$) where cellular detail could be resolved. Further examination with a narrower FOV setting (25°) revealed one additional layer (Fig. $5B_1$) that was unnoticed with the 55° FOV setting. Figs. $5A_2$-F_2 show smaller ROIs (~6.25°) that have been digitally cropped from the 25° FOV image and expanded to provide a magnified view of cellular detail. Figs. $5A_3$-F_3 pinpoints the approximate locations in the SDOCT B-scans where SLO GFP+ signal originates.

At an SLO focus of ~50-60 D, we observed the VRI (Figs. $5A_0$-A_1). These features were easily distinguishable as being retinal vessels (devoid of GFP signal), Müller glia endfeet (green), and ganglion cell axons (interdigitating between Müller glia signal). A change (Δ = - 20 D) in focus reveals the GCL where GFP positive Müller glial processes surround the large ganglion cell nuclei (Figs. $5B_1$-B_2). At 40 D, punctate hyperfluorescent spots corresponding to Müller glia processes can be observed in Figs. $5C_1$-C_2 in the IPL (Franze et al., 2007). As the SLO focus is advanced further into the INL (Figs. $5D_0$-D_2) Müller cell soma can be visualized. (Fig. $5D_3$). Advancing the SLO focus past the somas into the OPL (Figs. $5E_0$-E_2) reveals the distal Müller glia processes (Fig. $5E_3$). Finally, in the ONL/cone mosaic layer, the GFP signal is seen surrounding the photoreceptors (dark spots) (Figs. $5F_0$-F_2).

We used this optical sectioning method to characterize microglia from the *Tg(mpeg1:EGFP)* zebrafish. Images obtained from the *Tg(mpeg1:EGFP)* line are shown in Fig. 6 and show both native IR reflectance data of the VRI and cone mosaic (Figs. 6A-B) and GFP+ cellular morphology of microglia and/or macrophages collected at various locations throughout the retina (Figs. 6C-F). Individual GFP+ microglia (Figs. 6G-J) are shown within a region of interest (ROI) obtained from Figs. 6C-F. ROIs show that the cellular morphology can be distinguished and is different between inner (Figs. 6G-I) and outer retina (Fig. 6J) regions. These observed morphological differences are reminiscent of inflammatory monocytes in resting (i.e. extended dendrites) vs. active (i.e. engorged cell bodies with retracted dendrites) states. A ROI from a full width SDOCT B-scan (not shown) of a *Tg(mpeg1:EGFP)* zebrafish is shown in Fig. 6K along with a corresponding SDOCT LRP (Fig. 6L). The VRI, cone mosaic, and GFP+ microglia data (Fig. 6L; brackets) observed in five *Tg(mpeg1:EGFP)* using IR- (Figs. 6A-B) and AF-SLO (Figs. 6C-F) is plotted alongside the LRP from one

animal. This graph demonstrates that SLO can approximate the in-depth locations of GFP+ inflammatory cells within the retina. The majority of cells were primarily clustered in the IPL and OPL of the retina, but also were occasional observed in the outer retina (Fig. 6F).

Comparison of SLO Imaging in Zebrafish vs. Other Mammalian Eyes

Table 2 shows a summary of the reported differences in axial length and refractive power of zebrafish (Collery et al., 2014) vs. humans (Delori et al., 2011; Heidelberg, 2006a, b; Malaraca-Hernandez and Malaraca-Hernandez, 2003), rats (Chaudhuri et al., 1983) and mice (Remtulla and Hallett, 1985). As the eye gets smaller both axial and focal lengths are reduced concomitantly. Moreover, ocular power and image magnification increase substantially as these parameters become smaller. SLO raster scans and FOV's that are ~7-15 mm in diameter in humans are reduced as axial length decreases. This results in estimated raster scan density increases of 77, 88 and 94% for rats, mice and zebrafish over humans. Digital pixel separation reported for the HRA2 system in humans using a 55° wide field lens is reported to be on the order of ~10 μm (Heidelberg, 2006b). Assuming a linear change related to axial length, one can calculate the estimated digital pixel separation for rats, mice and zebrafish (Table 2). Figure 7 shows a set of experiments conducted to compare and contrast the primary parameters influencing image collection and display of zebrafish retina versus rodents and humans. From these experiments, parameters such as focus span, focus translation rate and lateral and confocal depth of field were estimated for the various species lenses that are commonly imaged using the HRA2 and Spectralis family of scanning laser confocal imaging systems.

SLO Focus Span and Focus Translation Rate

Focus span determined by *in vivo* imaging of a cohort of zebrafish, mice and rats demonstrated that focus span increases exponentially (R^2=0.995) with decreasing axial length (Fig. 7A). Essentially, more rotations of the focus knob are required to advance the image plane through the retina in smaller vs. larger eyes. Combining the span data with complimentary in-depth information acquired by SDOCT enabled us to calibrate the SLO focus adjustment in terms of axial distance relative to refractive power. Fig. 7A demonstrates that the focus translation rate increases substantially as the eye becomes smaller. This change was found to be linear (R^2=0.993) over the span of refractive powers present in the three species of animals investigated. The focus translation rate determined for zebrafish, mice and rats was 0.87, 4 and 12 μm/D, respectively.

SLO Image Lateral Resolution

SLO lateral image resolution was estimated for rats, mice and zebrafish after imaging four commercially available glass lenses with known refractive power. Measurements from these lenses permitted generation of the MTF plot shown in Fig. 7B. The plot shows how image contrast decreases as line spacing interval becomes smaller. Further demonstrated is the influence of increasing lens refractive power and its ability to resolve smaller spacing intervals. The lenses chosen for generating the MTF plot spanned the range of previously reported whole eye refractive powers for rats (Remtulla and Hallett, 1985) and mice (Chaudhuri et al., 1983) and are displayed in Table 2. The whole eye refractive power for

zebrafish is an estimate calculated from the focal length reported by Collery et al. (Collery et al., 2014).

Fig. 7B shows the maximum resolvable line spacing interval that could be observed from the 1951 USAF target with each of the four glass lenses. A reference threshold of 10% contrast was chosen to determine the minimum resolvable line pair for each lens shown in Fig. 7C. With the 1363 D lens, the smallest calibration interval (645.1 lp/mm) was resolvable and thus the 10% contrast value was extrapolated after performing a linear curve fit of the data. Fig. 7C shows that image resolution improves exponentially with increasing dioptric power and appears to be approaching an asymptote at ~ 1.5 μm. As one would anticipate, the estimated lateral resolutions found in retinas of different species are predominately influenced by the refractive powers of their respective ocular systems.

SLO Confocal Depth of Field (DOF)

SLO confocal DOF was estimated using a similar approach to that aforementioned for obtaining lateral resolution. DOF results for the four glass lenses are displayed in Fig. 7D. As observed, confocal DOF narrowed with increasing dioptric power. DOF at full-width half-maximum (FWHM) is plotted as a function of refractive power for each lens in Fig. 7E. FWHM DOF decreased linearly with increasing refractive power. From this curve fit, one can estimate the DOF for humans, rodents or zebrafish if the whole eye refractive power is known. An improvement in confocal DOF of field is observed when imaging small animals, such as rats (>10%) and mice (~30%) compared to humans, with this difference becoming substantial (~50%) as one moves to imaging zebrafish.

Discussion

In this report we have demonstrated the capabilities and limitations involved with performing *in vivo* optical sectioning of the adult zebrafish retina using two, well-established imaging devices. SLO could be used to identify two structures, VRI and photoreceptors, within the retina, which served as anatomical landmarks. These structures, and their locations, are similar to those observed in mice, with exception to the latter, where the RPE/choroid is discernible in small mammals (Paques et al., 2006; Seeliger et al., 2005) instead of photoreceptor rows. In zebrafish, punctate hyper-reflective or hypo-reflective foci, depending on the imaging modality used (i.e. IRDF-SLO or SDOCT), could be visualized which we have suspected originate from photoreceptors. As previously shown in retinal flat mounts (Allison et al., 2010) and by *in vivo* fundus imaging (Duval et al., 2013), the elongated ring feature circumscribing the optic disk appears to demarcate the larval remnant where cone photoreceptors transition from unorganized to organized rows. Photoreceptors observed in the periphery were much easier to resolve and could be seen in a highly organized state. In these regions, additional lines of reflective foci could be seen that suggests the insertion of additional photoreceptor cell rows being produced as the animal and/or eye increases in size. As previously shown by Nishiwaki et al. in the medaka eye (Nishiwaki et al., 1997), intercalated lines could be observed inserted between existing photoreceptor rows. Our results are very similar to those of Nishiwaki suggesting that we are

indeed visualizing some aspect of the cone mosaic using both SLO and SDOCT imaging modalities.

It was possible to collect both visible and infrared autofluorescence information using AF- and IRAF-SLO to complement the IR reflective information. Although not quantified, this information lacked appreciable detail and appeared relatively weak compared to images obtained by our group and others in mice which have been shown to indicate lipofuscin accumulation (Sparrow et al., 2013), melanin content (Charbel Issa et al., 2012) and the presence of inflammatory monocytes (Luhmann et al., 2009). These weaker signal amplitudes could also be attributed in part to zebrafish having smaller pupils (~50%) than those of dilated mice. Pupil diameter has been previously shown to influence SLO signal collection efficiency in mice (Charbel Issa et al., 2012). On the other hand, the weak signal observed by AF-SLO in wild type animals was advantageous when examining transgenic animals with GFP fluorescence. In this situation, one can be assured that the signal being observed is exclusive to the fluorescent protein and not to native tissue autofluorescence.

As previously demonstrated by Bailey et al., SDOCT of the zebrafish retina could be obtained including identification of prominent lamina. Bailey et al. showed that bright and dark signal bands in SDOCT B-scans correlated well to histology, but they did not elaborate on the highly structured region within the outer retina that contains photoreceptors. Within this region resides the photoreceptor mosaic, with its tiered, crystalline-like arrangement of rod and cone photoreceptor types. We aimed to elucidate the complex reflective architecture observed by SDOCT within this region. By using two independent SDOCT systems we converted the two-dimensional B-scan images into longitudinal reflectance profiles and compared them to a “to scale” model of adult zebrafish photoreceptors (Branchek and Bremiller, 1984). Reflective foci, spaced apart in ~10-15 micrometer increments (e.g. in the axial, in-depth direction) within this region, appear to denote the proximal and distal reflections from IS/OS interfaces and apical tips of cone photoreceptors. Theoretical models of the human photoreceptor layer have long proposed that the proximal (IS/OS or ellipsoid zone) and distal aspects of cone outer segments (COST line) are a source of SDOCT reflections originating from within this region (Jonnal et al., 2010; Pallikaris et al., 2003; Zhang et al., 2006). SDOCT B-scans acquired using the two independent imaging systems and their corresponding LRPs are in good agreement with the architecture and anatomical dimensions previously reported for zebrafish cone photoreceptors (Branchek and Bremiller, 1984; Hodel et al., 2006; Raymond et al., 1993).

As demonstrated in Figures 5 & 6, integration of SLO and SDOCT imaging data proved fruitful. This exercise demonstrated that manually performed optical sectioning (i.e. pseudo-tomography) of zebrafish retina using commercially available SLO and SDOCT ocular imaging systems can be realized. Calibration of the SLO axial focus adjustment using information obtained from the SDOCT imaging enabled co-registration of reflective and fluorescent information collected independently via the two imaging systems. Without co-registration and overlay of this information, it would be difficult to ascertain where fluorescent protein signal originates in the SLO image stack and with what retinal layer it should associate to in SDOCT B-scan. Worth noting, however, is that this technique was primarily limited to the inner retina. SLO imaging contrast and information yield within the

outer retina, and more specifically the cone mosaic, was not as successful. Fluorescent targets (Müller glia and macrophages) imaged from within the inner retina were spaced apart rather conveniently compared to those found in the cone mosaic of the outer retina. The close packing arrangement and stacked nature of cone mosaic, accompanied by the presence of the melanin pigment band that limits light penetration, presents a formidable challenge to resolve when SLO lateral and axial depth of field resolution are ~1.8 and 150 μm, respectively.

To our knowledge, the change in SLO imaging properties (i.e. resolution) that can occur when transitioning from larger to smaller mammals or fish with different ocular powers has not been previously reported. After imaging multiple research animals with this instrument, we observed that clarity and detail of certain retinal structures (e.g. nerve fiber layer and vascular network with IR-SLO) is improved as one transitions from rats, to mice, and then on to zebrafish (Suppl. Fig. 4). We were curious to determine how much improvement in resolution and depth of field could be realized within these three different research species relative to what has been reported for humans. As the eye becomes smaller, axial length gets shorter and the refractive power of the ocular system increases. Using raster-scanned instruments like SLO and SDOCT, smaller eyes with short axial lengths result in higher raster scan densities than observed with human eyes. Spherical ball lenses, which are the dominant refractive element in the zebrafish eye, are often employed to focus collimated, monochromatic light from lasers into single mode optical fibers that are a few to several μm in diameter. SLO utilizes monochromatic light from lasers to perform a raster scan of the retina. In the human eye, the Spectralis/HRA2 instrument has been reported to produce a spot size of ~ 10 μm on the retina (Delori et al., 2011). However, lateral resolution essentially approaches an asymptotic limit that is limited to and defined by many complex optical criteria within both the optical system of the instrument as well as animal being imaged. To further our understanding of what type of resolution exists between imaging humans, rodents and zebrafish we performed a series of experiments to define the anticipated lateral resolution and confocal depth of field in each of these animal subjects.

This study has further expanded the crucial role that non-invasive *in vivo* imaging plays in assessment of small animal models. By using these two devices in a harmonious manner, we have been able to image several zebrafish strains and characterize individual subjects throughout the duration of an experiment. Important to note is that we have observed differences in what was expected with some transgenic lines, including animals with pre-existing abnormalities at baseline, some strains with higher rates of abnormalities than others and last, unexpected and/or uncharacterized GFP expression phenotypes. The imaging techniques and approaches outlined within this framework can provide invaluable information to assist with screening and maintaining experimental zebrafish colonies in a non-destructive and non-invasive manner.

Supplementary Material

Refer to Web version on PubMed Central for supplementary material.

Acknowledgments

We thank Prof. Nusslein-Volhard and Francesca Peri for providing the *Tg(apoeb:lynEGFP)* zebrafish line and Dr. Yuankai Tao for providing the custom-built SDOCT imaging system. The study was supported in part by National Institutes of Health Grants 1K08EY023608-04 and R01EY017037, minority supplement from the National Eye Institute (RO1EY017037-09S1), an unrestricted grant from Research to Prevent Blindness, Research to Prevent Blindness Doris and Jules Stein Professorship, a Foundation Fighting Blindness Research Center Grant, The Wolf Family Foundation, the Llura and Gordon Gund Foundation, and the Cleveland Clinic.

References

Allison WT, Barthel LK, Skebo KM, Takechi M, Kawamura S, Raymond PA. Ontogeny of cone photoreceptor mosaics in zebrafish. J Comp Neurol. 2010; 518:4182–4195. [PubMed: 20878782]

Alvarez Y, Cederlund ML, Cottell DC, Bill BR, Ekker SC, Torres-Vazquez J, Weinstein BM, Hyde DR, Vihtelic TS, Kennedy BN. Genetic determinants of hyaloid and retinal vasculature in zebrafish. Bmc Developmental Biology. 2007; 7:114. [PubMed: 17937808]

Bailey TJ, Davis DH, Vance JE, Hyde DR. Spectral-domain optical coherence tomography as a noninvasive method to assess damaged and regenerating adult zebrafish retinas. Invest Ophthalmol Vis Sci. 2012; 53:3126–3138. [PubMed: 22499984]

Beck SC, Schaeferhoff K, Michalakis S, Fischer MD, Huber G, Rieger N, Riess O, Wissinger B, Biel M, Bonin M, Seeliger MW, Tanimoto N. In vivo analysis of cone survival in mice. Invest Ophthalmol Vis Sci. 2010; 51:493–497. [PubMed: 19737879]

Bell BA, Kaul C, Bonilha VL, Rayborn ME, Shadrach K, Hollyfield JG. The BALB/c mouse: Effect of standard vivarium lighting on retinal pathology during aging. Exp Eye Res. 2015; 135:192–205. [PubMed: 25895728]

Bell BA, Kaul C, Rayborn ME, Hollyfield JG. Baseline imaging reveals preexisting retinal abnormalities in mice. Adv Exp Med Biol. 2012; 723:459–469. [PubMed: 22183365]

Bell BA, Xie J, Yuan A, Kaul C, Hollyfield JG, Anand-Apte B. Retinal vasculature of adult zebrafish: In vivo imaging using confocal scanning laser ophthalmoscopy. Exp Eye Res. 2014; 129:107–118. [PubMed: 25447564]

Bilotta J, Saszik S. The zebrafish as a model visual system. International Journal of Developmental Neuroscience. 2001; 19:621–629. [PubMed: 11705666]

Boudard DL, Tanimoto N, Huber G, Beck SC, Seeliger MW, Hicks D. Cone loss is delayed relative to rod loss during induced retinal degeneration in the diurnal cone-rich rodent Arvicanthis ansorgei. Neuroscience. 2010; 169:1815–1830. [PubMed: 20600653]

Branchek T, Bremiller R. The development of photoreceptors in the zebrafish, Brachydanio rerio. I. Structure. J Comp Neurol. 1984; 224:107–115. [PubMed: 6715574]

Charbel Issa P, Barnard AR, Singh MS, Carter E, Jiang Z, Radu RA, Schraermeyer U, MacLaren RE. Fundus autofluorescence in the Abca4(-/-) mouse model of Stargardt disease--correlation with accumulation of A2E, retinal function, and histology. Invest Ophthalmol Vis Sci. 2013; 54:5602–5612. [PubMed: 23761084]

Charbel Issa P, Singh MS, Lipinski DM, Chong NV, Delori FC, Barnard AR, MacLaren RE. Optimization of in vivo confocal autofluorescence imaging of the ocular fundus in mice and its application to models of human retinal degeneration. Invest Ophthalmol Vis Sci. 2012; 53:1066–1075. [PubMed: 22169101]

Chaudhuri A, Hallett PE, Parker JA. Aspheric curvatures, refractive indices and chromatic aberration for the rat eye. Vision Res. 1983; 23:1351–1363. [PubMed: 6666037]

Chauhan BC, Stevens KT, Levesque JM, Nuschke AC, Sharpe GP, O'Leary N, Archibald ML, Wang X. Longitudinal in vivo imaging of retinal ganglion cells and retinal thickness changes following optic nerve injury in mice. PLoS One. 2012; 7:e40352. [PubMed: 22768284]

Chhetri J, Jacobson G, Gueven N. Zebrafish[mdash]on the move towards ophthalmological research. Eye. 2014; 28:367–380. [PubMed: 24503724]

Collery RF, Veth KN, Dubis AM, Carroll J, Link BA. Rapid, accurate, and non-invasive measurement of zebrafish axial length and other eye dimensions using SD-OCT allows longitudinal analysis of myopia and emmetropization. PLoS One. 2014; 9:e110699. [PubMed: 25334040]

Delori F, Greenberg JP, Woods RL, Fischer J, Duncker T, Sparrow J, Smith RT. Quantitative measurements of autofluorescence with the scanning laser ophthalmoscope. Invest Ophthalmol Vis Sci. 2011; 52:9379–9390. [PubMed: 22016060]

DiCicco RM, Bell BA, Kaul C, Hollyfield JG, Anand-Apte B, Perkins BD, Tao YK, Yuan A. Retinal regeneration following OCT-guided laser injury in zebrafish. Invest Ophthalmol Vis Sci. 2014; 55:6281–6288. [PubMed: 25205862]

Duval MG, Chung H, Lehmann OJ, Allison WT. Longitudinal fluorescent observation of retinal degeneration and regeneration in zebrafish using fundus lens imaging. Mol Vis. 2013; 19:1082–1095. [PubMed: 23734077]

Franze K, Grosche J, Skatchkov SN, Schinkinger S, Foja C, Schild D, Uckermann O, Travis K, Reichenbach A, Guck J. Muller cells are living optical fibers in the vertebrate retina. Proc Natl Acad Sci U S A. 2007; 104:8287–8292. [PubMed: 17485670]

Gloesmann M, Hermann B, Schubert C, Sattmann H, Ahnelt PK, Drexler W. Histologic correlation of pig retina radial stratification with ultrahigh-resolution optical coherence tomography. Invest Ophthalmol Vis Sci. 2003; 44:1696–1703. [PubMed: 12657611]

Hassenstein A, Meyer CH. Clinical use and research applications of Heidelberg retinal angiography and spectral-domain optical coherence tomography - a review. Clin Experiment Ophthalmol. 2009; 37:130–143. [PubMed: 19338610]

Heidelberg. Heidelberg Retina Angiograh 2 Operating Instructions. 2006a:48.

Heidelberg. Software v2.0 Automatic Real Time (ART) 55° Wide Field Objective. Germany: 2006b. Heidelberg Retina Angiograph 2 Release Notes; p. 1-7.

Hodel C, Neuhauss SC, Biehlmaier O. Time course and development of light adaptation processes in the outer zebrafish retina. Anat Rec A Discov Mol Cell Evol Biol. 2006; 288:653–662. [PubMed: 16721865]

Hossain P, Liversidge J, Cree MJ, Manivannan A, Vieira P, Sharp PF, Brown GC, Forrester JV. In vivo cell tracking by scanning laser ophthalmoscopy: quantification of leukocyte kinetics. Invest Ophthalmol Vis Sci. 1998; 39:1879–1887. [PubMed: 9727411]

Hughes V. Will This Fish Transform Medicine? Popular Science. 2013

Hwang WY, Fu Y, Reyon D, Maeder ML, Tsai SQ, Sander JD, Peterson RT, Yeh JR, Joung JK. Efficient genome editing in zebrafish using a CRISPR-Cas system. Nat Biotechnol. 2013; 31:227–229. [PubMed: 23360964]

Jiao S, Ruggeri M, Wehbe H, Gregory G, Jockovich ME, Hackam A, Puliafito CA. Imaging of eye tumor in the mouse model of retinoblastoma with spectral-domain optical coherence tomography - art. no. 64260D. Ophthalmic Technologies XVII. 2007; 6426:D4260–D4260.

Jonnal RS, Besecker JR, Derby JC, Kocaoglu OP, Cense B, Gao W, Wang Q, Miller DT. Imaging outer segment renewal in living human cone photoreceptors. Optics Express. 2010; 18:5257–5270. [PubMed: 20389538]

Joshi R, Pankova N, Wang H, Baek DS, Zhao X, Reyad M, Boyd SR. Spontaneously occurring fundus findings observed using confocal scanning laser ophthalmoscopy in wild type Sprague Dawley rats. Regul Toxicol Pharmacol. 2016; 77:160–166. [PubMed: 26873774]

Luhmann UF, Robbie S, Munro PM, Barker SE, Duran Y, Luong V, Fitzke FW, Bainbridge JW, Ali RR, MacLaren RE. The drusenlike phenotype in aging Ccl2-knockout mice is caused by an accelerated accumulation of swollen autofluorescent subretinal macrophages. Invest Ophthalmol Vis Sci. 2009; 50:5934–5943. [PubMed: 19578022]

Maass A, von Leithner PL, Luong V, Guo L, Salt TE, Fitzke FW, Cordeiro MF. Assessment of rat and mouse RGC apoptosis imaging in vivo with different scanning laser ophthalmoscopes. Curr Eye Res. 2007; 32:851–861. [PubMed: 17963105]

Malaraca-Hernandez, D.; Malaraca-Hernandez, Z. Handbook of Optical Design. 3rd. CRC Press; 2003.

Mattapallil MJ, Wawrousek EF, Chan CC, Zhao H, Roychoudhury J, Ferguson TA, Caspi RR. The Rd8 mutation of the Crb1 gene is present in vendor lines of C57BL/6N mice and embryonic stem cells, and confounds ocular induced mutant phenotypes. Invest Ophthalmol Vis Sci. 2012; 53:2921–2927. [PubMed: 22447858]

McLellan GJ, Rasmussen CA. Optical coherence tomography for the evaluation of retinal and optic nerve morphology in animal subjects: practical considerations. Veterinary Ophthalmology. 2012; 15:13–28. [PubMed: 22805095]

Nishiwaki Y, Oishi T, Tokunaga F, Morita T. Three-dimensional reconstitution of cone arrangement on the spherical surface of the retina in the medaka eyes. Zoological Science. 1997; 14:795–801.

Thévenaz P, R UE, Unser M. A Pyramid Approach to Subpixel Registration Based on Intensity. IEEE Transactions on Image Processing. 1998; 7(1):27–41. [PubMed: 18267377]

Pallikaris A, Williams DR, Hofer H. The reflectance of single cones in the living human eye. Investigative Ophthalmology and Visual Science. 2003; 44:4580–4592. [PubMed: 14507907]

Paques M, Simonutti M, Roux MJ, Picaud S, Levavasseur E, Bellman C, Sahel JA. High resolution fundus imaging by confocal scanning laser ophthalmoscopy in the mouse. Vision Res. 2006; 46:1336–1345. [PubMed: 16289196]

Peri F, Nusslein-Volhard C. Live imaging of neuronal degradation by microglia reveals a role for v0-ATPase a1 in phagosomal fusion in vivo. Cell. 2008; 133:916–927. [PubMed: 18510934]

Rao KD, Verma Y, Patel HS, Gupta PK. Non-invasive ophthalmic imaging of adult zebrafish eye using optical coherence tomography. Current Science. 2006; 90:1506–1510.

Rauscher FG, Azmanis P, Korber N, Koch C, Hubel J, Vetterlein W, Werner B, Thielebein J, Dawczynski J, Wiedemann P, Reichenbach A, Francke M, Krautwald-Junghanns ME. Optical coherence tomography as a diagnostic tool for retinal pathologies in avian ophthalmology. Invest Ophthalmol Vis Sci. 2013; 54:8259–8269. [PubMed: 24282225]

Raymond PA, Barthel LK, Curran GA. Developmental patterning of rod and cone photoreceptors in embryonic zebrafish. J Comp Neurol. 1995; 359:537–550. [PubMed: 7499546]

Raymond PA, Barthel LK, Rounsifer ME, Sullivan SA, Knight JK. Expression of rod and cone visual pigments in goldfish and zebrafish: a rhodopsin-like gene is expressed in cones. Neuron. 1993; 10:1161–1174. [PubMed: 8318234]

Remtulla S, Hallett PE. A schematic eye for the mouse, and comparisons with the rat. Vision Res. 1985; 25:21–31. [PubMed: 3984214]

Robinson J, Schmitt EA, Harosi FI, Reece RJ, Dowling JE. Zebrafish ultraviolet visual pigment: absorption spectrum, sequence, and localization. Proc Natl Acad Sci U S A. 1993; 90:6009–6012. [PubMed: 8327475]

Rosolen SG, Saint-MacAry G, Gautier V, Legargasson JF. Ocular fundus images with confocal scanning laser ophthalmoscopy in the dog, monkey and minipig. Vet Ophthalmol. 2001; 4:41–45. [PubMed: 11397318]

Samuels IS, Bell BA, Sturgill-Short G, Ebke LA, Rayborn M, Shi L, Nishina PM, Peachey NS. Myosin 6 is required for iris development and normal function of the outer retina. Invest Ophthalmol Vis Sci. 2013; 54:7223–7233. [PubMed: 24106123]

Seeliger MW, Beck SC, Pereyra-Munoz N, Dangel S, Tsai JY, Luhmann UF, van de Pavert SA, Wijnholds J, Samardzija M, Wenzel A, Zrenner E, Narfstrom K, Fahl E, Tanimoto N, Acar N, Tonagel F. In vivo confocal imaging of the retina in animal models using scanning laser ophthalmoscopy. Vision Res. 2005; 45:3512–3519. [PubMed: 16188288]

Sparrow JR, Blonska A, Flynn E, Duncker T, Greenberg JP, Secondi R, Ueda K, Delori FC. Quantitative fundus autofluorescence in mice: correlation with HPLC quantitation of RPE lipofuscin and measurement of retina outer nuclear layer thickness. Invest Ophthalmol Vis Sci. 2013; 54:2812–2820. [PubMed: 23548623]

Toth CA, Narayan DG, Boppart SA, Hee MR, Fujimoto JG, Birngruber R, Cain CP, DiCarlo CD, Roach WP. A comparison of retinal morphology viewed by optical coherence tomography and by light microscopy. Arch Ophthalmol. 1997; 115:1425–1428. [PubMed: 9366674]

Tschopp M, Takamiya M, Cerveny KL, Gestri G, Biehlmaier O, Wilson SW, Strahle U, Neuhauss SCF. Funduscopy in Adult Zebrafish and Its Application to Isolate Mutant Strains with Ocular Defects. PLoS One. 2010; 5

Westerfield, M. The Zebrafish Book. 5th. University of Oregon Press; Eugene, Oregon: 2007.

Zhang QX, Lu RW, Messinger JD, Curcio CA, Guarcello V, Yao XC. In vivo optical coherence tomography of light-driven melanosome translocation in retinal pigment epithelium. Sci Rep. 2013; 3:2644. [PubMed: 24025778]

Zhang Y, Cense B, Rha J, Jonnal RS, Gao W, Zawadzki RJ, Werner JS, Jones S, Olivier S, Miller DT. High-speed volumetric imaging of cone photoreceptors with adaptive optics spectral-domain optical coherence tomography. Optics Express. 2006; 14:4380–4394. [PubMed: 19096730]

Highlights

- A model is proposed explaining the outer retina banding pattern seen in zebrafish with high resolution SDOCT
- By combining SLO and SDOCT imaging data, we demonstrate the ability to optically section through the retina
- Integration of retina data collected in vivo from two independent imaging systems revealed detailed and depth-resolved information on retinal morphology
- We demonstrate how imaging small animals changes SLO axial and transverse resolution and confocal depth of field

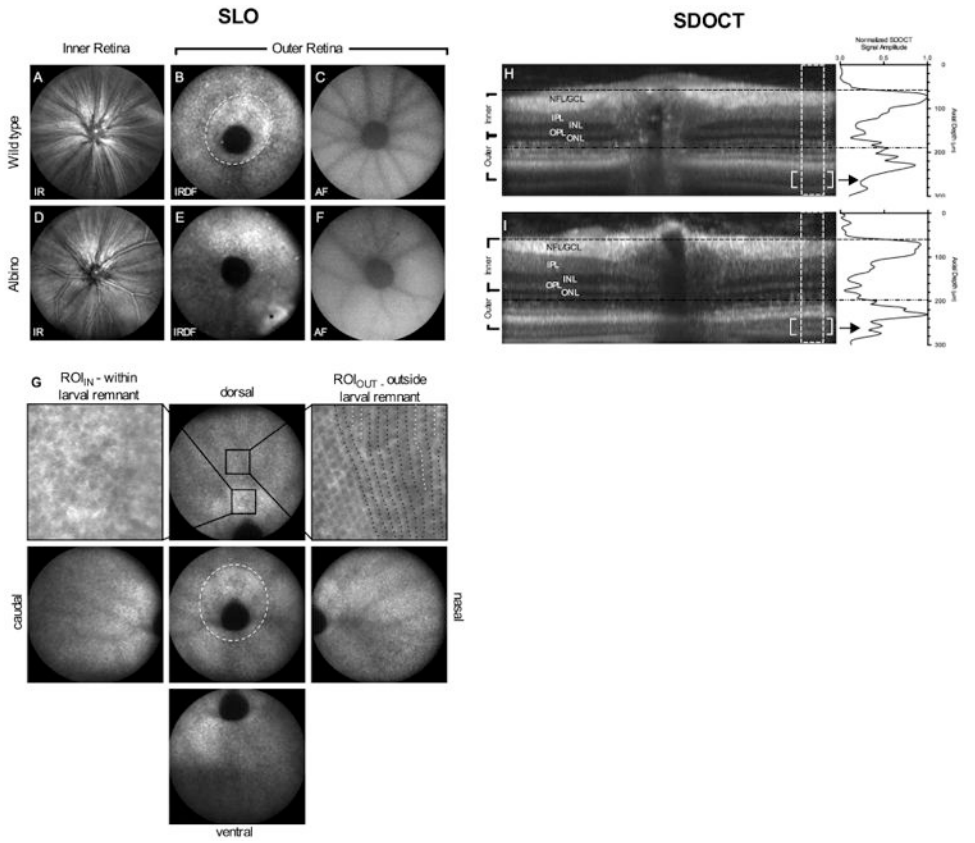

Figure 1.

SLO and SDOCT images of retina from pigmented and albino zebrafish. IR reflectance images from the VRI (A, D). IRDF images from outer retina showing the optic disk and photoreceptor mosaic (B, E). Central and peripheral IRDF-SLO views acquired from a wild type fish (G) showing that photoreceptor organization is more easily discerned with increasing distance from the optic disk. Black arrows in the central view outline the larval remnant where photoreceptor morphology transitions from a disorganized to organized architecture between 20 and 36 dpf. Regions of interest from within (upper left) and outside (upper right) of the larval remnant are shown to reveal the hyporeflective nature of short single UV cones, the most proximal (i.e. vitreal aspect) of the three cone types found within this region. Within the larval remnant photoreceptors appear randomly distributed (upper left; arrows). In contrast, an ROI from outside the larval remnant shows hyporeflective short single cones appearing as spots oriented in vertical rows (upper right; black dotted lines). In this ROI, intercalation of new photoreceptor rows that occur as a result of animal growth can be visualized (upper right; white dotted lines) Native autofluorescence (488nm excitation/ 500-680 emission) images from the outer retina (C, F). SDOCT images show the similarities and/or differences between the in-depth morphology of pigmented (H) and albino (I) animals. Horizontal lines indicate the approximate locations where the VRI (H; black hashed lines) and outer retina (I; black hashed-dot-dot lines) that have been previously shown in SLO images (A, D and B, E), respectively. The lack of melanin pigment within melanosomes (M) of RPE apical processes in albino animals improves light penetration and imaging depth over pigmented animals (Fig. 1D vs. 1H; enclosed brackets). Within this

region, additional structural detail can be discerned within the outer retina such as rod outer segments (ROS) and retinal pigment epithelium (RPE). Image dimensions: (A-F) ~1mm, (G) standard views ~ 1 mm and ROI_{IN} & ROI_{OUT} ~ 0.13mm), & (H-I) - 0.3 mm (depth) × ~1 mm (width).

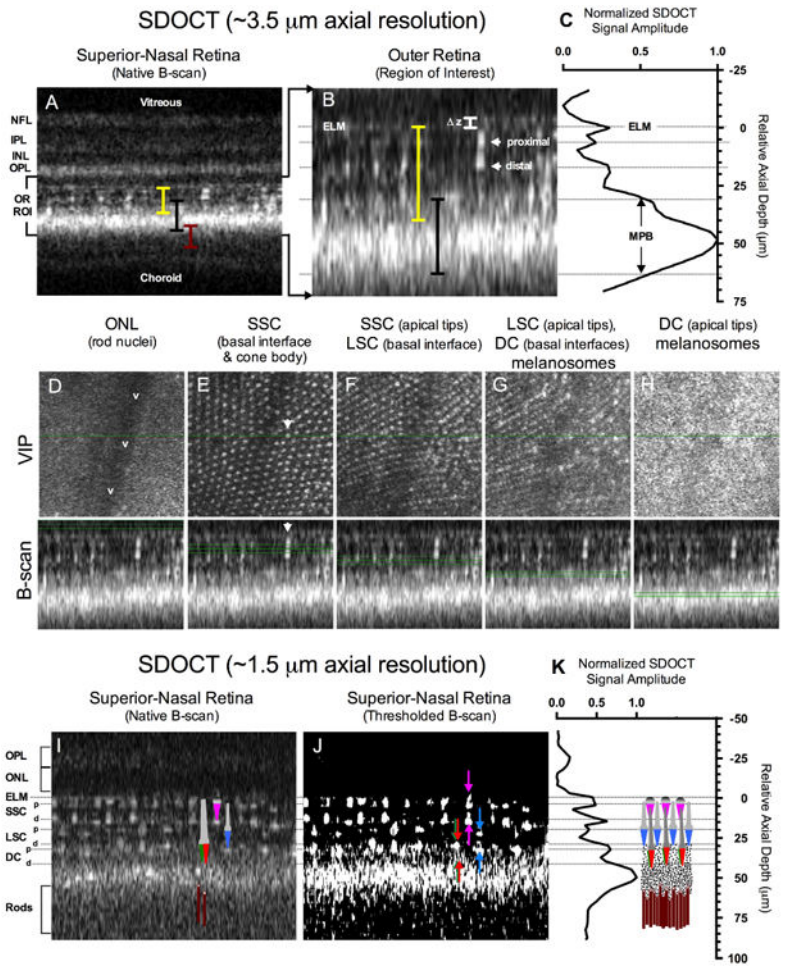

Figure 2.

SDOCT of the zebrafish outer retina using high (A-H) and ultra-high axial resolution (I-K). A full thickness B-scan (A) shows the approximate locations (colored bars) of the cone mosaic (yellow), melanin pigment zone (black), and rod outer segments (maroon). A magnified view of the region of interest (B) shows reflections from the proximal and distal (i.e. apical) aspect of a single cone photoreceptor. The LRP (C) of the SDOCT ROI (B) shows the intensity distribution as a function of depth relative to the external limiting membrane. Figures 2D-H Volume Intensity Projections (VIP) corresponding to the B-scans obtained from the various locations (green lines) within the cone mosaic and MPB. Figures 2I-K show the improvements made in resolving the stacked cone layer architecture by increasing the axial resolution by ~ 3-fold. A color schematic of the zebrafish cone (SSC-magenta, LSC-blue, DC-Red/Green) and rod (maroon) photoreceptor types has been overlaid onto the B-scan image (Fig. 2I). A thresholded B-scan is provided in Fig. 2J to better accentuate the cone proximal (down arrows) and distal (up arrows) reflections. A LRP obtained from Fig. 2I is shown in Fig. 2K with a 1:1 scaled schematic of the zebrafish cone mosaic, MPB and rod outer segments adapted from Bracheck and Bremiller 1984 and Hodel et al. 2006. As can be observed in Fig. 2I, anatomical correlates to the ELM and cone proximal (b) and distal (a) tips are easily visible and align effortlessly with the model depicted in Fig. 2K. Increasing LRP reflectivity in the area of the double cones is apparent

and originates from melanosomes containing pigment granules. The pigment granules reach the point of highest density (LRP Maxima @ ~50 μm relative to the ELM in Fig. 2K) between the double cones and rod outer segments. SDOCT image dimensions are: (A) 0.3 mm (depth) × ~0.25 mm (width), (B) 0.085 mm (depth) × ~0.25 mm (width), (D-H) ~0.25 mm^2 (VIP window axes) by 0.085 mm (B-scan depth), and (I & J) 0.13 mm (depth) × ~0.25 mm (width).

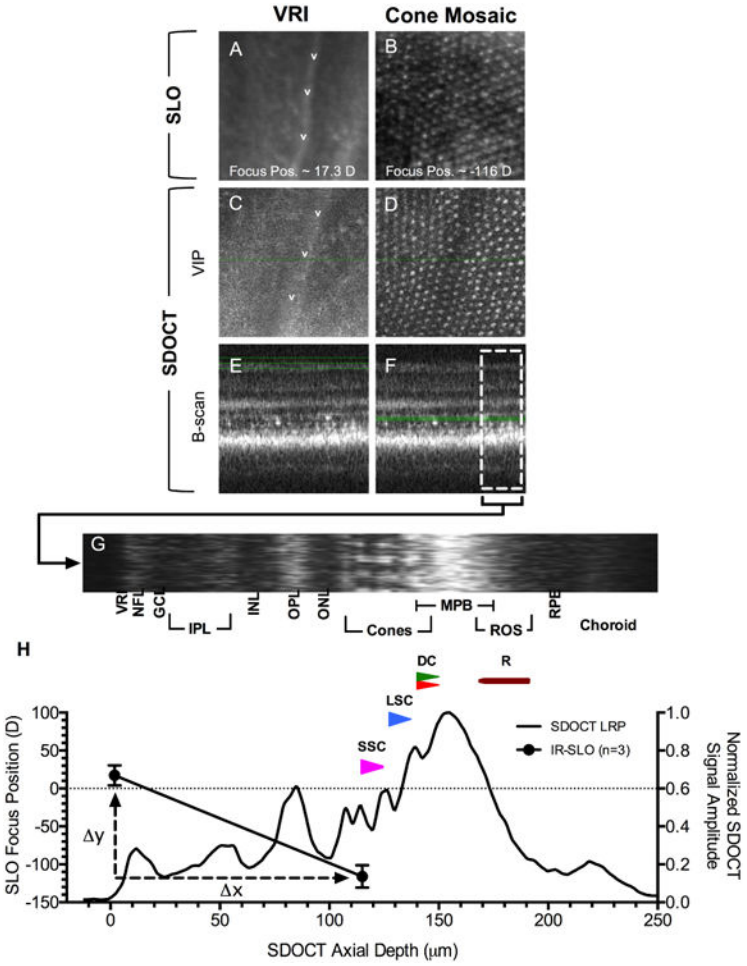

Figure 3.

Calibration of SLO focus position with SDOCT imaging data. *En face* views of the VRI and proximal cone mosaic using IR-SLO (A-B) and SDOCT (C-D). SDOCT VIPs for the VRI (C) and mosaic (D) were obtained from the regions bound by green lines shown (E & F), respectively. Fig. 3H shows an LRP obtained from the B-scan region of interest (F; white broken line box) that is rotated and displayed horizontally (G) above the graph. SLO focus position (mean±sd) in diopters for the VRI and cone mosaic is overlaid with the LRP data. SSC, LSC, DC, and rods are represented by magenta, blue, red/green, and maroon, respectively.

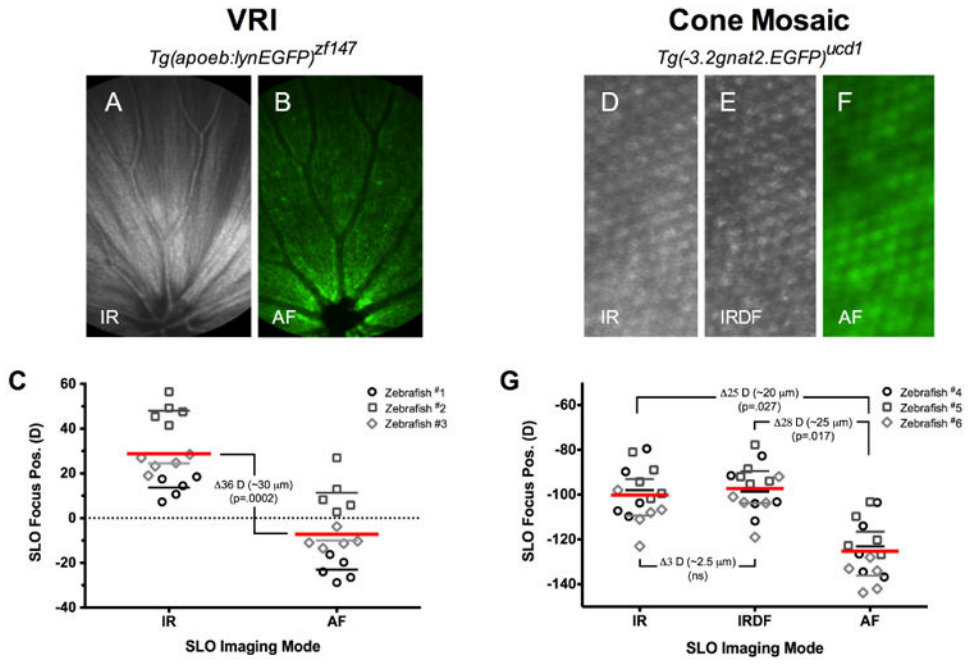

Figure 4.

The influence of chromatic aberration on SLO focus position. Fig. 4A-C shows results from an experiment conducted in *Tg(apoeb:lynEGFP)* animals to determine the amount of difference in optimal focus position between IR- (A) and AF-SLO (B) channels. This experiment was repeated using the cone mosaic from *Tg(-3.2gnat2:EGFP)* zebrafish. Optimal IR-, IRDF- and AF-SLO images of the cone mosaic (D-F). This data demonstrates that a chromatic aberration correction factor is necessary for display of IR and AF channel data in the same SLO/SDOCT data overlay. C and G summarizes the data obtained from 3 animals with average SLO focus position values for each modality. The chromatic aberration is similar at the VRI (C) and cone mosaic (G).

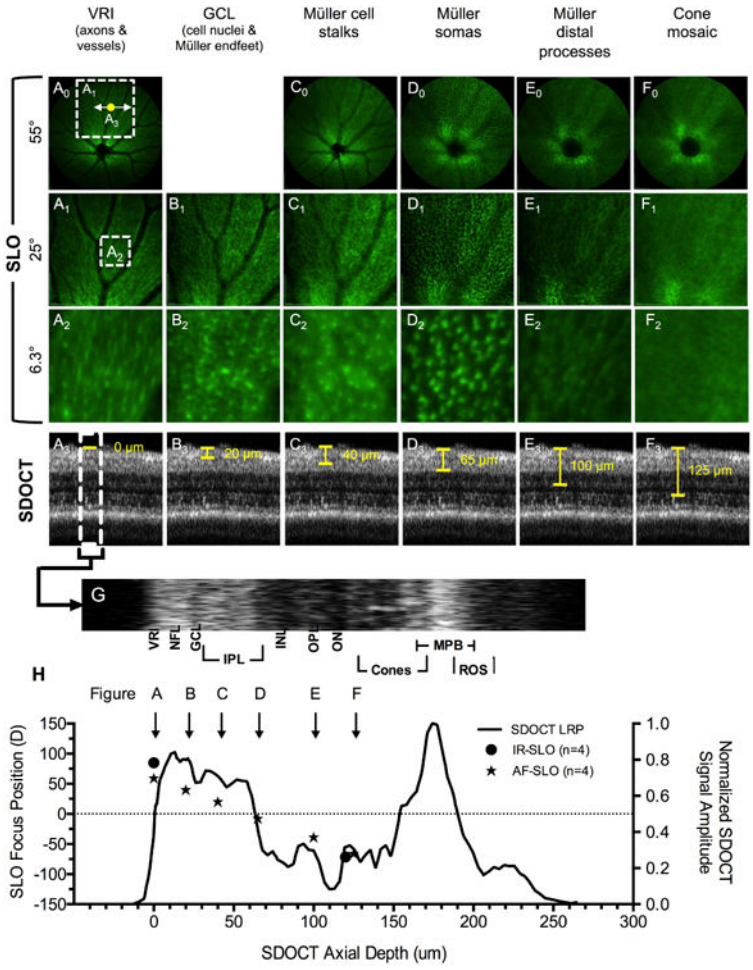

Figure 5.

In vivo optical sectioning in *Tg(apoeb:lynEGF)* zebrafish. Image planes from the VRI to the cone mosaic have been obtained using SLO field of views of 55° (A_0-F_0), 25° (A_1-F_1) and 6.3° (A_2-F_2). A_3-F_3 are SDOCT images from the corresponding location shown in A_0 (yellow dot). The SDOCT LRP (H) was obtained from the SDOCT ROI (G). An overlay of SLO and SDOCT data (H) shows the location of EGFP+ Müller Glia cell morphology identified by SLO relative to retinal lamina.

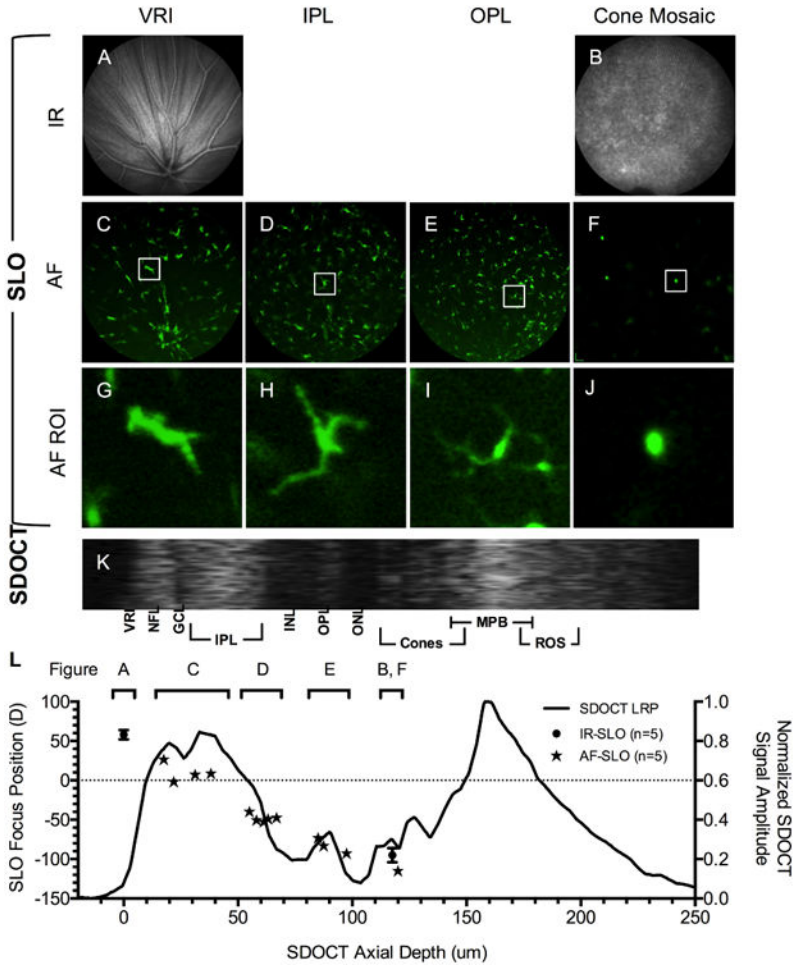

Figure 6.

In vivo optical sectioning of *Tg(mpeg1:EGFP)* extending from the VRI to the cone mosaic using IR- (A-B) and AF-SLO (C-F). Individual EGFP+ microglia have been isolated, digitally cropped, and expanded to better accentuate cellular detail (G-J). Figure 6K is an SDOCT ROI image from the same animal. The LRP (L) was obtained from the SDOCT ROI (K). An overlay of SLO and SDOCT data (K) shows the location of EGFP+ microglia cells identified by SLO relative to various retinal lamina. Data from multiple animals (n=5) are included to show population distributions of microglia cells within the retina. Zoomed views (G-J) demonstrate that SLO is capable of resolving dendritic processes and recognizing morphological differences in cells that are potentially in an active phagocytic (J) vs. resting state (G-I).

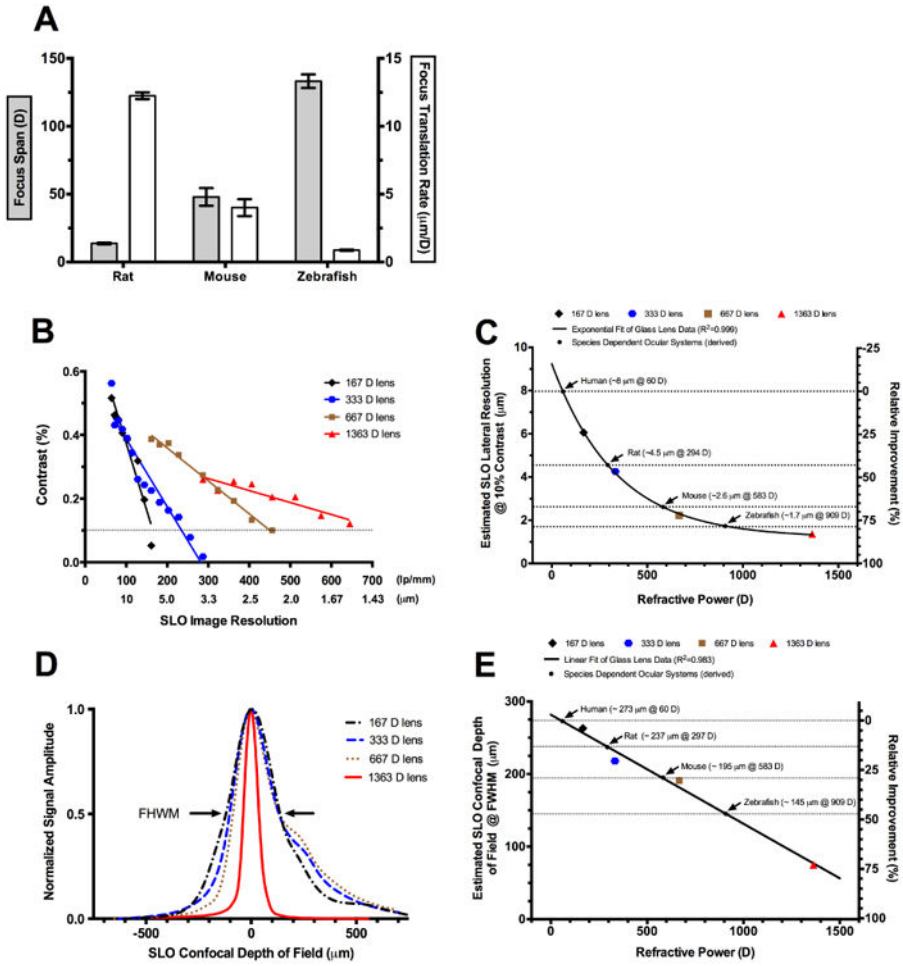

Figure 7.

SLO imaging parameters measured and/or derived for zebrafish as compared to other mammals such as humans and rodents. SLO focus span and focus translation rate measured for rats, mice and zebrafish (A). Lateral resolutions measured from a series of four different lenses with increasing refractive power (B). Lateral resolutions @ 10% MTF contrast for the four different lenses with species dependent ocular refractive powers inserted to estimate spatial resolution for humans, rats, mice, and zebrafish (C). Confocal depth of field (DOF) measured from a series of four different lenses with increasing refractive power (D). Estimated confocal DOF @ FWHM for the four different lenses shown plotted with a linear curve fit. The species dependent ocular refractive powers are shown inserted to estimate confocal DOF for humans, rats, mice, and zebrafish (E).

Table 1

Summary of zebrafish strains investigated

Zebrafish Strain	Fluorescent Label	N (#)
*Ekwill/AB** (wild type)	Not applicable – “wild type”	167
slc24a5$^{b1/b1}$ (AB)	Not applicable - “albino”	2
Tg(-3.2gnat2:EGFP)^{ucd1}	EGFP - cone photoreceptors	68
Tg(XlRho:EGFP)^{fl1}	EGFP - rod photoreceptors	18
Tg(apoeb:lynEGFP)^{zf147}	EGFP - Müller glial cells	50
Tg(mpeg1:EGFP)	EGFP - microglia	68
Tg(-5actb2:Arl13b-GFP)^{hsc5}	GFP - cilium	2
Tg(-5actb2:cetn4-GFP)^{cu6}	GFP - centrin	2

Table 2

Ocular parameters comparison between zebrafish and three different mammalian species. The table shows the influence of shortened axial length on front and back focal lengths, whole eye refractive power, estimated SLO field of view (FOV), change in raster scan density and estimated digital resolution. Italicized data are estimated and/or derived from other physical data parameters shown within the table.

Species	References	Axial Length (mm)	Front Focal Length (mm)	Back Focal Length (mm)	Whole Eye Power (D)	SLO FOV (mm)		Change in Scan Density (%)	Digital Pixel Separation (μm/pixel)
						55°	25°		
Human	(Delori et al., 2011; Heidelberg, 2006; Malaraca-Hernandez and Malaraca-Hernandez, 2003)	24.75	-16.7	22.891	60	*14.5*	*6.6*	-	~10
Rat	(Chaudhuri et al., 1983)	6.32	-3.351	4.483	294	*3.3*	*1.5*	*77%*	*~2.3*
Mouse	(Remtulla and Hallett, 1985)	3.379	-1.714	2.296	583	*1.8*	*0.8*	*88%*	*~1.2*
Zebrafish	(Collery et al., 2014)	1.69	*~1.1*	1.1	*~909*	*0.88*	*0.4*	*94%*	*~0.6*